Characterization and Modeling of Cell Wall Imperfections in Aluminum Honeycomb Cores Using X-Ray CT Imaging

Adrian X. Rivera[1] and Satchi Venkataraman[2]
[1,2] San Diego State University, San Diego, CA, 92182, US

Hyonny Kim[3]
[3]University of California, San Diego, CA, 92037, US

Evan Pineda[4]
[4]NASA Glenn Research Center, Cleveland, OH, 44135, US

Andrew Bergan[5]
[5]NASA Langley Research Center, Hampton, VA, 23666, US

Honeycomb cell imperfections, may significantly affect the failure of sandwich composites in core crushing and shear modes. Identification and quantification of the different types of imperfections and evaluation of their effects on the mechanical response of honeycomb cores in flatwise compression is presented. X-Ray computed tomography (CT) scans of honeycomb cores in co-cured composite sandwich panels were performed. Image analysis methods are applied to characterize and quantify core cell geometry and cell wall waviness. An approach is developed for extracting cell wall mid surface planes and waviness for constructing finite element models using shell elements. Analysis results from models with the as-manufactured imperfections are compared to results from models with idealized geometries to evaluate the effect of the as-manufactured imperfections on the initiation of cell wall buckling and subsequent core crushing.

I.   Introduction

The compression and bending strength of sandwich composites are significantly reduced by barely visible impact damage (BVID) in part due to crushing of the core material. Predicting the constitutive response of crushed cores requires developing detailed knowledge of the mechanisms that drive local core crushing deformations. Prior studies on BVID have focused on computational modeling to understand the strength reduction of the overall panel but have not fully investigated the deformation of the core, and the resulting residual stiffness and strength, after BVID [1]. Other studies have developed analytical expressions for strength predictions in honeycomb cores mapping failure to geometry variables in honeycomb core [2]. Prior studies on the effects of imperfections have used worse case imperfections taken from buckling modes. Actual imperfections are a signature of the manufacturing process used to produce the aluminum honeycomb and have a quasi-random expression. These as-manufactured imperfections have not been studied in detail, and their relation to compression strength or shear response of aluminum honeycomb core material is unclear at this time.

   Fig. 1 shows imperfections observed in a co-cured composite facesheet and aluminum honeycomb core sandwich panel. Imperfections are observed in the honeycomb core cell wall geometry such as cell shape distortion (Fig. 1), cell wall waviness, and cell wall thickness. The adhesive fillet that connects the core to the facesheet also presents its own imperfections such as variations in adhesive filet height and widths, porosities in the adhesive, and waviness of the composite facesheet (Fig. 2). Several of these imperfections can be attributed to the effects of manufacturing processes coupled with the material properties of the constituents. For example, the composite facesheets and honeycomb core material have very different coefficient of expansions (CTE). This CTE mismatch can lead thermal distortions in co-cured sandwich composites that can appear as cell wall geometry distortion and waviness via facesheet wrinkling or variation in fillet height formation [3,4]. The surface tension and viscosity of the adhesive during the cure process and

---

[1] PhD Student SDSU/UCSD Joint Doctoral Program in Structural Engineering, AIAA Member.
[2] Professor of Aerospace Engineering, AIAA Associate Fellow.
[3] Professor of Structural Engineering, AIAA Member.
[4] Research Engineer, Materials and Structures Branch, MS 49/7, AIAA Senior Member.
[5] Research Engineer, Durability, Damage Tolerance, and Reliability Branch, MS 188E, AIAA Senior Member.

the gravity field appear to affect the filet geometry shape (different on top and bottom face sheets with reference to the tool side). Variation in the honeycomb cell geometry such as cell diameter and the internal angles of the hexagonal cell shape can be traced in part to the extrusion of the honeycomb core material prior to the co-cure process. Sheets of aluminum foil are bonded, cut into strips, and then pulled (expanded) to take the honeycomb cell shape. Manufacturing process variability in producing these honeycomb cores can lead to size variations and internal angle variations (under or over expanded cells). Further cell distortions can also occur due to improper handling of the cores during the sandwich composite panel fabrication.

The objective of this paper is to develop procedures and algorithms to characterize and quantify geometric imperfections in honeycomb cores from X-Ray computed tomography (CT) imaging, develop finite element models of cores with such imperfections, and quantify effects of imperfections on the flatwise compressive response of sandwich panels. This is accomplished by utilizing image processing techniques to construct shell element meshes with as-manufactured geometries for honeycomb unit cells, and then comparing the results to models with idealized imperfections to evaluate the effects of imperfections on the flatwise compressive response.
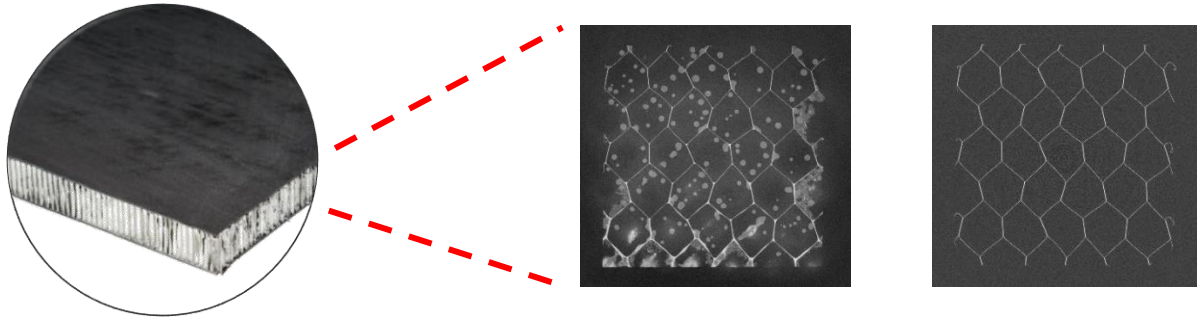

Fig. 1 Manufacturing imperfections in a co-cured aluminum honeycomb sandwich panel showing two slices of X-Ray CT data: at the facesheet/core interface showing porosity in adhesive filets and geometry distortion of hexagonal honeycomb cells.
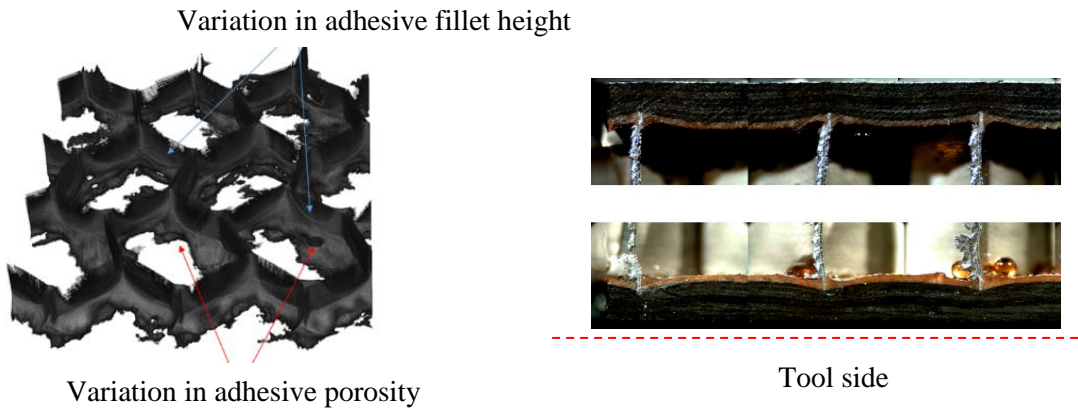
Variation in adhesive fillet height

Variation in adhesive porosity

Tool side

Fig. 2 Volume reconstruction of adhesive filets between facesheet and honeycomb core showing non-uniform filet formation and porosity and optical microscopy images of sandwich panel showing facesheet waviness and adhesive pooling due to the co-curing process.

II. Flatwise Compression Tests

A series of flatwise compression tests following ASTM C365 standard [5] were performed on two batches of 2"×2" sandwich specimens. The specimens were cut from two nominally identical sandwich panels with quasi-isotropic $[+45/90/-45/0]_s$ facesheets of IM7/8552 material and a 1.0-inch-thick Aluminum 5052 honeycomb core with a density of 3.1 pcf (lb/ft^3). While the materials and construction were nominally identical, the panels were fabricated at different NASA facilities, and the main differences appear to be between the two different batches of honeycomb cores. Nonetheless, the two batches of specimens capture a range of different manufacturing imperfections. The test

procedure followed the ASTM standard with quasi-static monotonic displacement controlled loading applied at a rate of 0.025 in/min. In addition to load and cross head displacement, full field deformation of one front face of the honeycomb was captured with digital image correlation (DIC).

Fig. 3 shows the nominal stress versus compressive displacement response from the tests. The samples are grouped by batch with red curves from the first batch, and the blue curves from the second batch, referred to here as batches B and R, respectively. The peak nominal compressive stress (i.e. strengths) vary significantly within the two batches as well as between the two batches. The range of strengths varies by approximately 15% within both batches. The difference in mean strengths between the batches is 35%. The relatively large difference in strength motivates the detailed study in the remainder of the paper to understand the most significant factors influencing the strength.
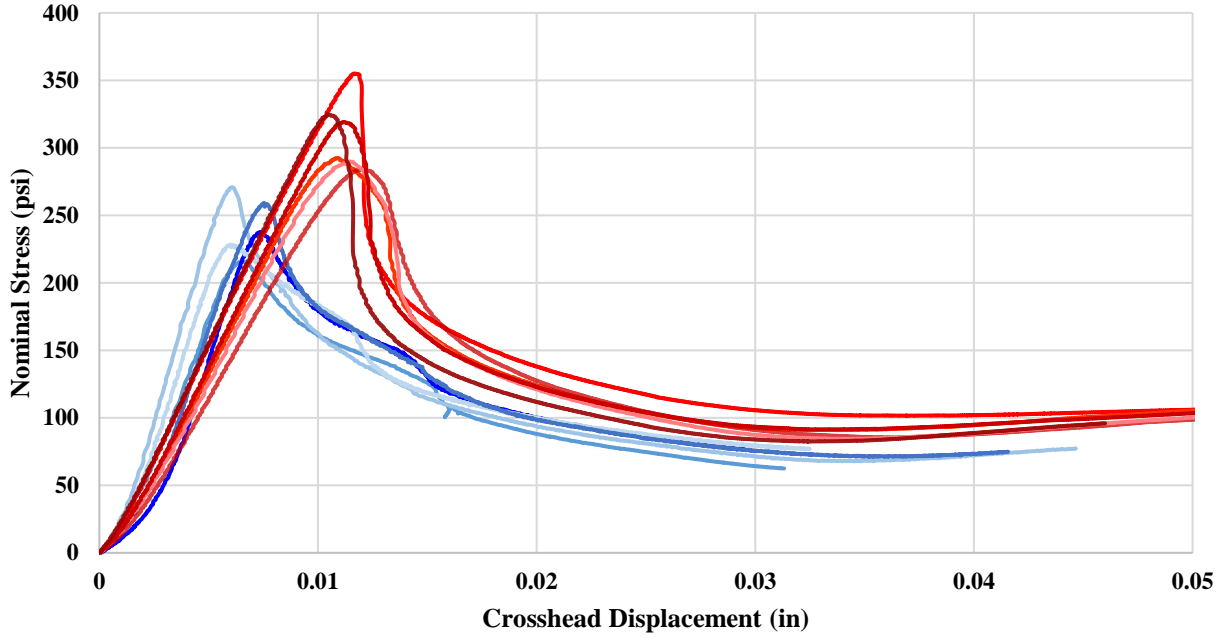

Fig. 3 Nominal stress versus compression displacement of two batches of specimens.

Prior to mechanical testing the specimens were imaged using X-Ray CT. The scans where conducting using a X-RAY WorX 80 watt source and a Dexela 2923 detector configured such that the source was 200 mm from the specimen and 760 mm from the detector. The scans captured 1800 projections resulting in 1410 image slices through the thickness of the specimen (1.085") and a typical voxel size of 20 μm. The honeycomb core cell wall geometry at the midplane from the specimens with the largest compression strength in each batch are shown in Fig. 4. These CT slices show that each individual cell within a test specimen has unique geometric features. To quantify these geometric features, image processing techniques were used to better understand similarities and differences between the two batches of specimens, as described in the next section.
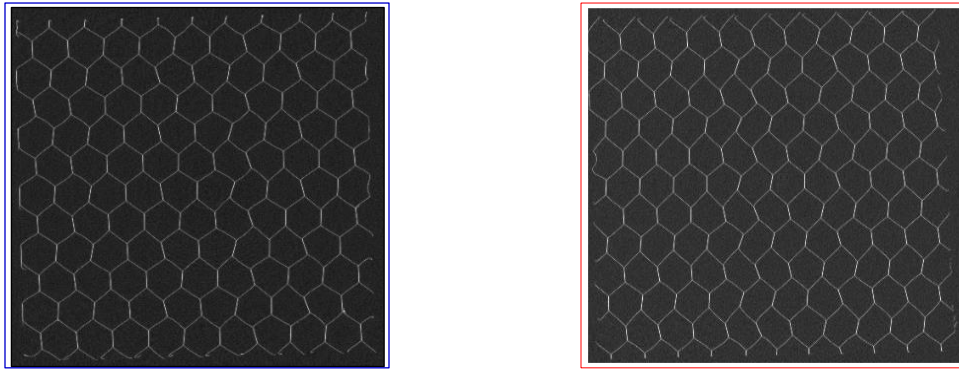

Fig. 4 X-ray CT slices from batch B and batch R, respectively.

3

Out-of-plane displacement DIC data taken from a representative specimen in batch B just prior to collapse is shown in Fig. 5. Local regions of large out-of-plane displacements appear in each cell suggesting that imperfections have driven cell wall buckling and post-buckling localization and plastic deformation is starting. This supports the hypothesis that the particular buckling and post-buckling response of each specimen is influenced by the specimen's geometric imperfections, based on the literature on buckling of thin wall shell structures [6]. However, the DIC is only able to give surface images of the response along the edge of the specimen, which may be influenced by incomplete cell geometry and distortions created when cutting the specimens to size.
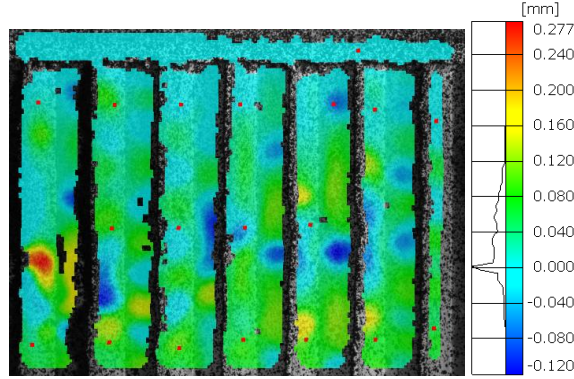

Fig. 5 Out-of-plane displacement measured using digital image correlation on the end face of a flatwise compression specimen just prior to collapse (peak load).

III. Analysis of Geometric Imperfections of the Honeycomb Cells

The pre-test X-Ray CT scans were analyzed using image processing techniques to quantify a set of metrics describing the geometric imperfections of the honeycomb. A typical cell is shown in Fig. 6 where it can be seen that the cell deviates is several respects from an ideal hexagon. The selected geometric features that were investigated are cell diameter, cell internal angles, and cell wall waviness since these metrics are both quantifiable from the X-Ray CT data and potentially significant in terms of the flatwise compression strength. The cell wall thickness may also vary, but such variations could not be measured from the X-Ray CT scans due to the resolution. This section describes the results of the honeycomb cell geometric analysis for the three selected metrics.
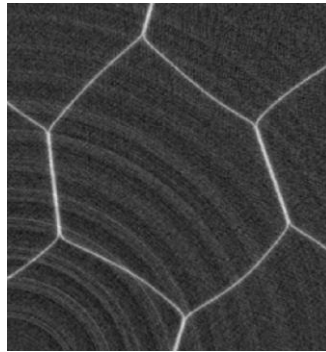

Fig. 6 A typical cell imaged with X-Ray CT.

A. Cell Diameter
The cell diameters were extracted from CT slices normal to the thickness direction. The image processing steps used inlcude, thresholding [7], to convert greyscale image to a binary image, filtering using a wavelet filter [8] to remove imaging artifacts, and finally a 2D marching square algorithm [9] for edge detection. The results are then analyzed to extract parametric geometry information. All the cells in one sample from each batch were analyzed except the open

cells at the free edges of the specimen. The cell diameter is defined as the distance between the center of the double thickness cell walls of each individual cell. For this honeycomb, the nominal cell diameter is 0.1875 inches. Histograms of cell diameters for the two batches are shown in Fig. 7. The histograms show that the batch B specimens have larger diameters, while the batch R specimens have smaller diameters, when compared to nominal cell diameter. In other words, the honeycomb used in batch B was overexpanded with an average diameter of 0.1905 inches while batch R was underexpanded with an average diameter of 0.1798 inches. The same trends are shown for four specimens summarized in the box plot Fig. 8 where any results outside of two standard deviations are considered outliers and shown with circular markers. From Fig. 8 it is clear that batch B has significantly more outliers than batch R.
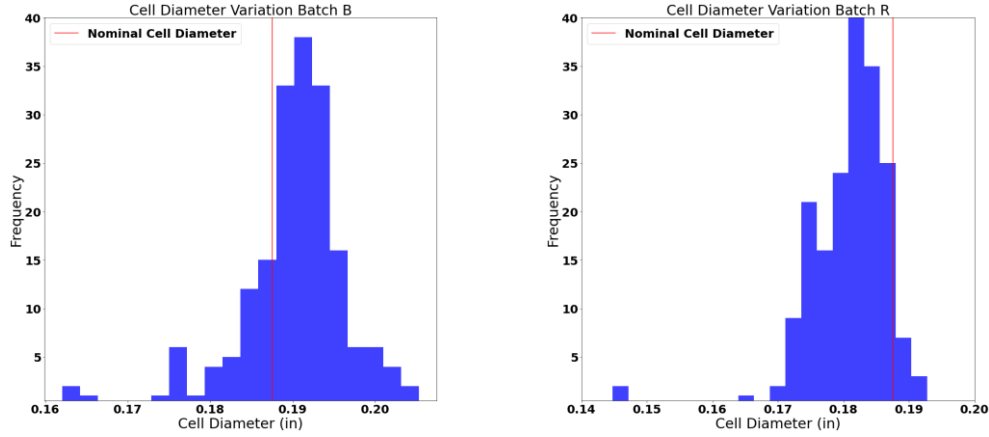

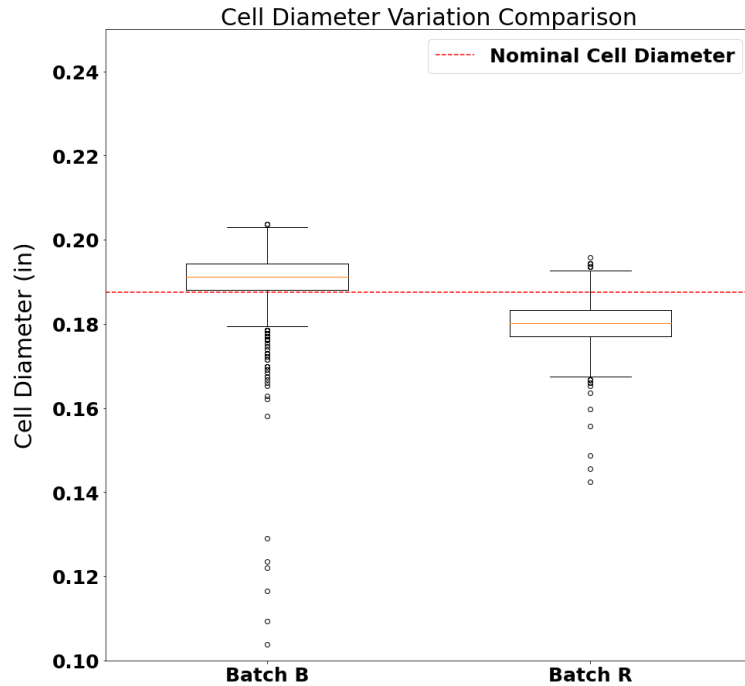**Fig. 7 Histogram plot showing cell diameter from a single specimen of each batch.**

Fig. 8 Box plot showing cell diameter distribution from a four specimens of each batch.

B. Cell Angles
Internal cell angles were calculated by considering three points where one point was selected on each cell wall and third point was located at the corner. Since the cell walls are wavy, the points on the cell walls were selected near the corners. Fig. 9 describes the internal cell angle numbering scheme; furthermore, this designation is used to identify the cell wall locations relative to the ribbon direction.
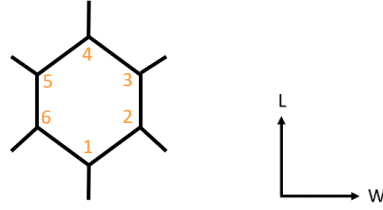
Fig. 9 Diagram showing the defined angle locations.

The results are shown in a box plot in Fig. 10 where a relatively similar trend is noted in the results from the two batches. In both batches, there is a consistent trend of large values for θ_3 and θ_6, which suggests that there is a systematic rotation of the double cell walls. Table 1 highlights the means at each angle location. Consistent with the cell diameter, the internal cell angle data shows more outliers in batch B than batch R.
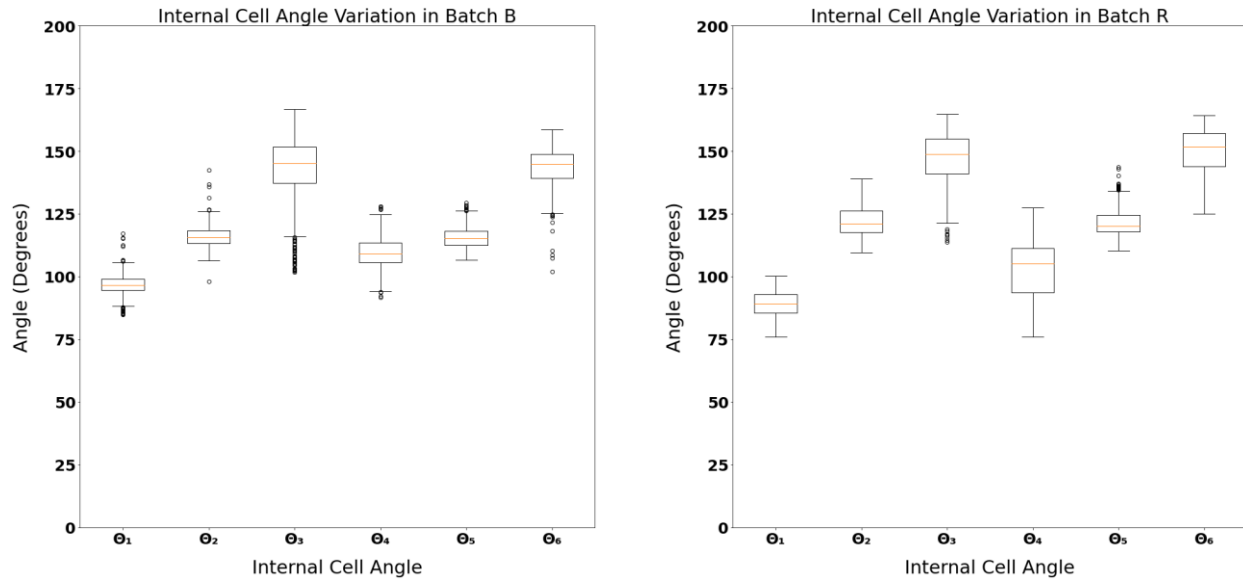

Fig. 10 Box plot showing the internal angle distributions from four samples of each batch.

Table 1. The mean of the internal angle and percent difference between batch B and bacth R specimens.

Internal Angles	θ_{1B}	θ_{2B}	θ_{3B}	θ_{4B}	θ_{5B}	θ_{6B}	θ_{1R}	θ_{2R}	θ_{3R}	θ_{4R}	θ_{5R}	θ_{6R}
Mean (deg.)	96.7	116.0	143.0	109.5	115.9	143.7	89.3	121.8	146.8	102.9	121.4	150.5
Percent Difference B-R	-7.65	5.00	2.66	-6.01	4.74	4.73						

C. Cell Wall Waviness

Cell wall waviness was analyzed by taking sections along the thickness direction through the center of each cell wall. Since the X-Ray CT data resolution was such that the cell walls included only two voxels, the resulting data was relatively noisy and piecewise. Distinct differences in cell wall waviness were noticed comparing the "single cell walls" (cell walls 1-2, 3-4, 4-5, 6-1) to the "double cell walls" (cell walls 2-3, 5-6). The amplitude of the cell wall waviness is summarized in the histograms for the single cell walls and double cell walls in Fig. 11. The histograms show generally much higher amplitudes of cell wall waviness in the single cell walls compared with the double cell walls. The number of instances in which the amplitude was > 0.004 inches the single cell walls was over 1200, while for that same range the double cell walls had less than 10 instances. This can be attributed to single cell walls having half the foil thickness making them more succeptible to deformation during the curing and expansion processes.
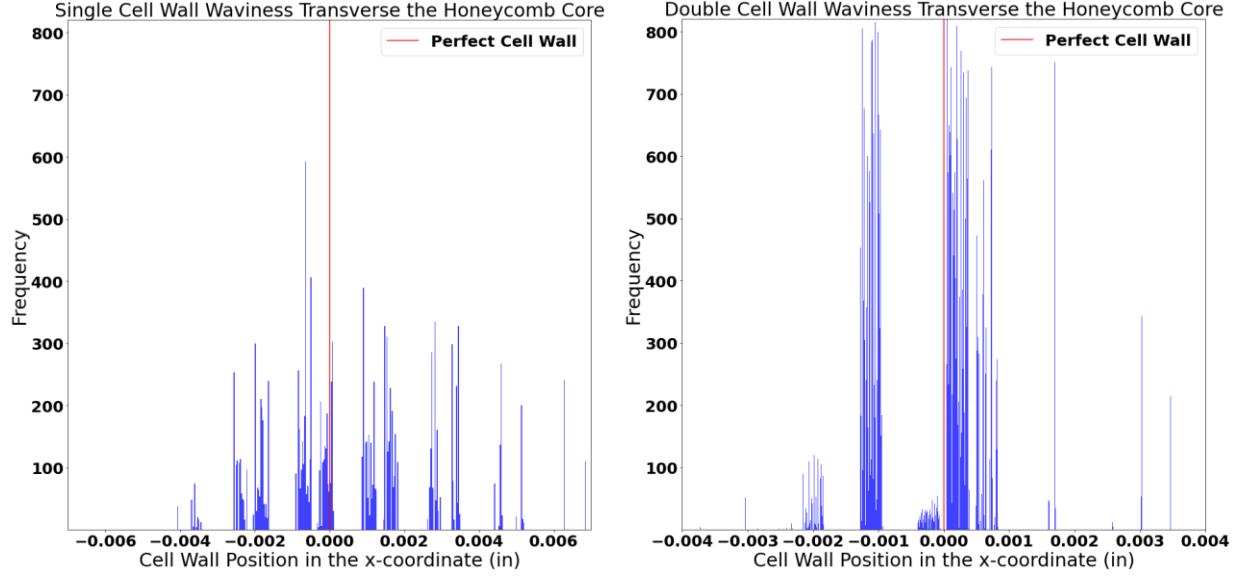
Fig. 11 Histograms showing cell wall waviness amplitude.

IV. As-manufactured Mesh Creation

The X-Ray CT data can be used to directly reconstruct a mesh containing the as-manufactured imperfections. Existing approaches rely on a two-step process where, first, a point cloud representing the geometry of interest is obtained via segmentation, and then, a point cloud reconstruction algorithm such as ball pivot is used to obtain a mesh. The existing approaches are mostly focused on obtaining 3D solid geometry and meshes. For computational efficiency, a shell representation of the honeycomb is preferred. Attempts to adapt the conventional reconstruction approach described above to the current data proved challenging, resulting in poorly defined meshes with gaps and overlaps. To overcome these difficulties, a hybrid approach was used, as illustrated in Fig. 12. The point cloud was simplified to obtain a set of points representing the cell wall mid-planes at a specified number of slices through-the-thickness of the core. The points were fit with splines at each slice and then surfaces were fit through the splines. Finally, the surfaces were meshed with quadrilateral (shell) elements. The resultant mesh captures the cell wall curvature, cell diameter, and cell internal angles well while also creating a regular mesh. Future work should evaluate the accuracy of the reconstruction procedure.
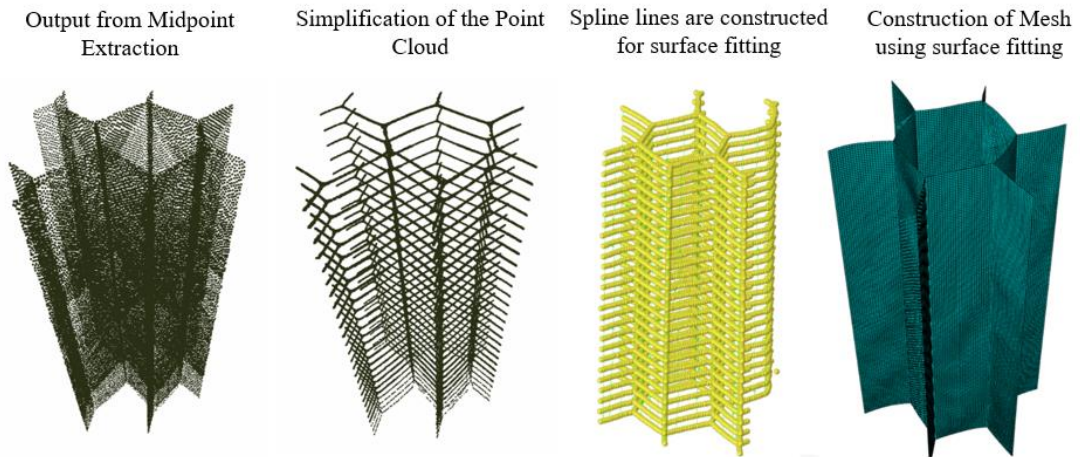

Fig. 12 Workflow for creating an as-manufactured mesh of a honeycomb cell.

V. Finite Element Analysis of Honeycomb Unit Cells

A series of unit-cell finite element analyses were conducted to understand the correlation between geometric imperfections and the flatwise compression response. Models were constructed using the geometric imperfections measured in batch B and batch R as well as idealized imperfections from the eigenvalue buckling mode shapes. An image of the mesh, the nominal dimensions of the model, and the boundary conditions are shown in Fig. 13. The model was discretized with linear reduced-integration shell (S4R) elements with a typical size of 0.005 inches. While the nominal core thickness in the tests was 1.0 inch, the models are 0.8 inch thick since only the region between the adhesive fillets is considered. The boundary conditions on "free" cell walls are symmetric. While periodic boundary conditions might be preferred, the non-periodic as-manufactured imperfections made it impossible to enforce periodicity appropriately. Perfect plasticity was assumed in the model using the experimental data reported by Lerch [10], which is for the same foil material as in the flatwise test specimens. The data in reference [10] shows hardening behavior very close to perfectly plastic. The models were analyzed using Abaqus/Standard [11] with an implicit dynamic step.
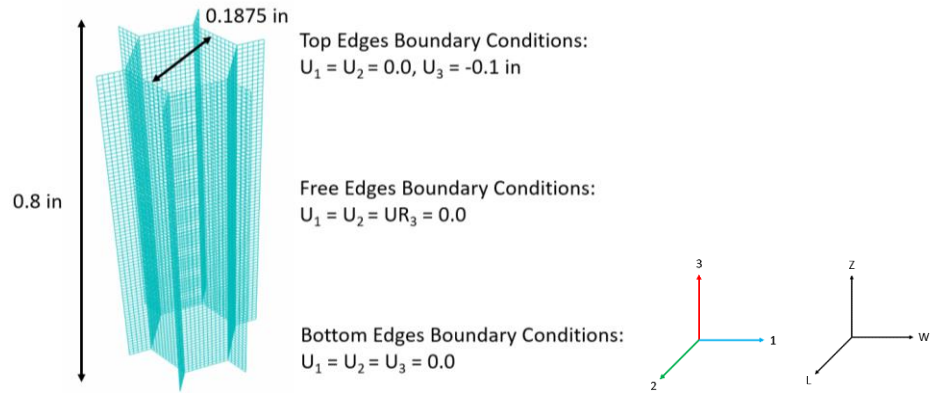

Fig. 13 Diagram of the idealized unit cell model with the geometric features and boundary conditions with reference to the global and material coordinate system.

Four geometries were analyzed as summarized in Table 2. The first two cases included idealized cell wall waviness imperfections obtained from the first eigenvalue buckling mode shape shown in Fig. 14. In these two cases, the cell diameter and cell angles were the nominal values. In the first case, the imperfection amplitude was scaled to the average waviness amplitude (0.00132 inches) from the geometric imperfection analysis above. In the second case, the imperfection amplitude was from a peak amplitude of a unit cell near the center of a specimen representative of batch R. The last two cases were the models with as-manufactured imperfections for one specimen from each batch.

Table 2. Summary of geometries of the unit cell models [10].

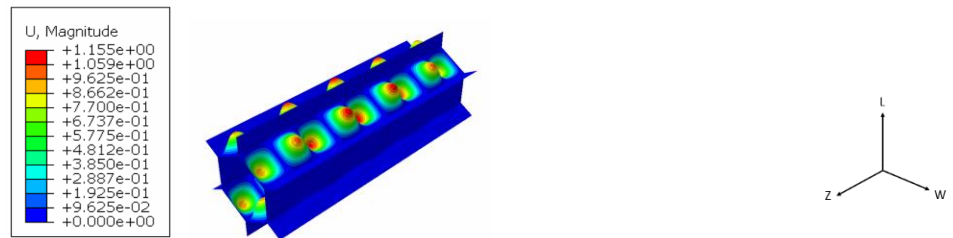|	Cell Diameter (in)	Cell Height (in)	θ_1 (°)	θ_2 (°)	θ_3 (°)	θ_4 (°)	θ_5 (°)	θ_6 (°)
Ideal Average	0.1875	0.8	120	120	120	120	120	120
Ideal Peak	0.1875	0.8	120	120	120	120	120	120
Batch B	0.1833	0.8	111	146	102	126	126	109
Batch R	0.1774	0.8	87	138	126	107	116	146

Fig. 14 First buckling mode shape.

Fig. 15 shows nominal compressive stress versus displacement curves from the four models. The compression response shows a linear elastic region followed by pre-peak hardening, load drop due to cell wall buckling, and a stable post-buckling collapse (crushing) of the core. Table 3 summarizes the peak nominal stresses that indicates the compression strength of the honeycomb cores analyzed. The idealized unit cell with average amplitude had the highest strength (ultimate nominal stress). The percent difference between the two idealized unit cell models is 44.7 percent. Therefore, the magnitude of the applied imperfection significantly effects the compression strength of the unit cell models. The unit cell based on batch R has a compression strength that is 12.6 percent higher than the unit cell based on batch B. Based on these results, it is observed that an imperfection scaled to the average waviness does not accurately capture the knockdown in compression strength. It is also noteworthy that the imperfections affect the pre-peak and post-peak response.
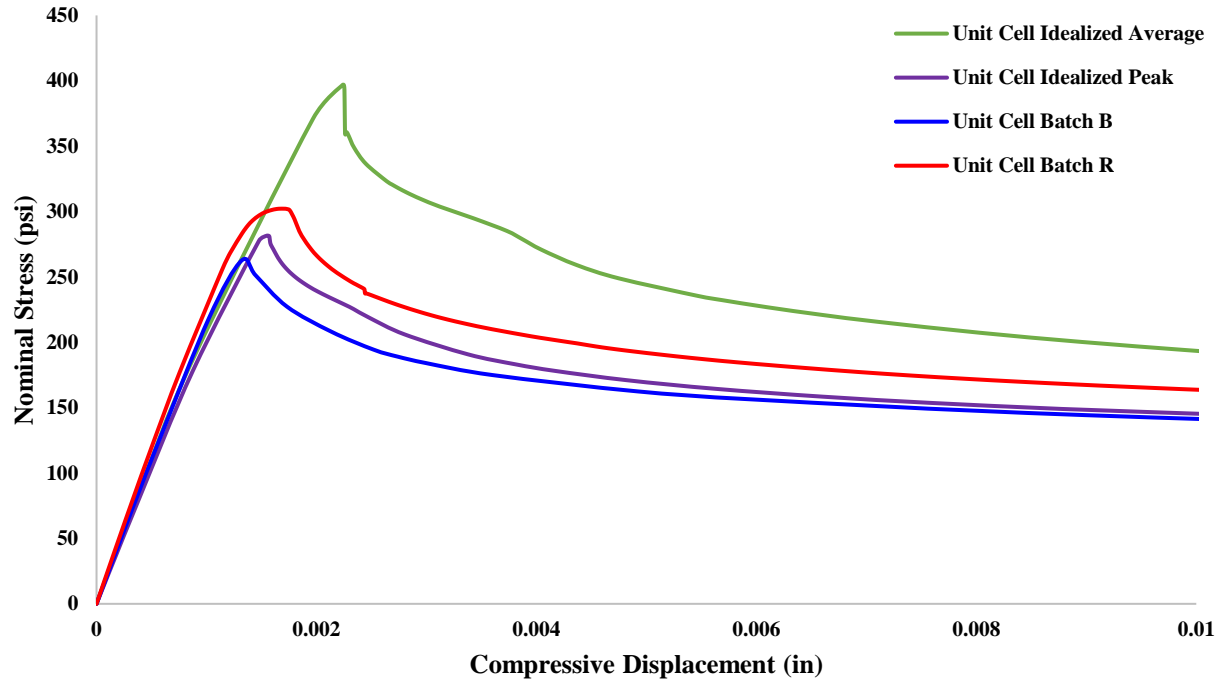

Fig. 15 Nominal compressive stress versus displacement from the unit cell models.

Table 3. Summary of Finite Element Results.

	Peak Nominal Stress (psi)	*Failure Location Height (in)*
Ideal Unit Cell Scaled to Average	396	0.400
Ideal Unit Cell Scaled to Peak	276	0.130
Batch B Unit Cell	268	0.163
Batch R Unit Cell	302	0.471

The contour plots shown in Fig. 16 compare magnitude of deformations on the cell wall at load step before collapse. These contour plots also show the location of the maximum cell wall deformation. In both idealized models, the initiation of collapse occurs in the double thickness cell walls that align with the ribbon direction. In both cases for the unit cells analyzed with as-manufactured imperfections quantified from CT show the initiation of the collapse in the single cell walls.
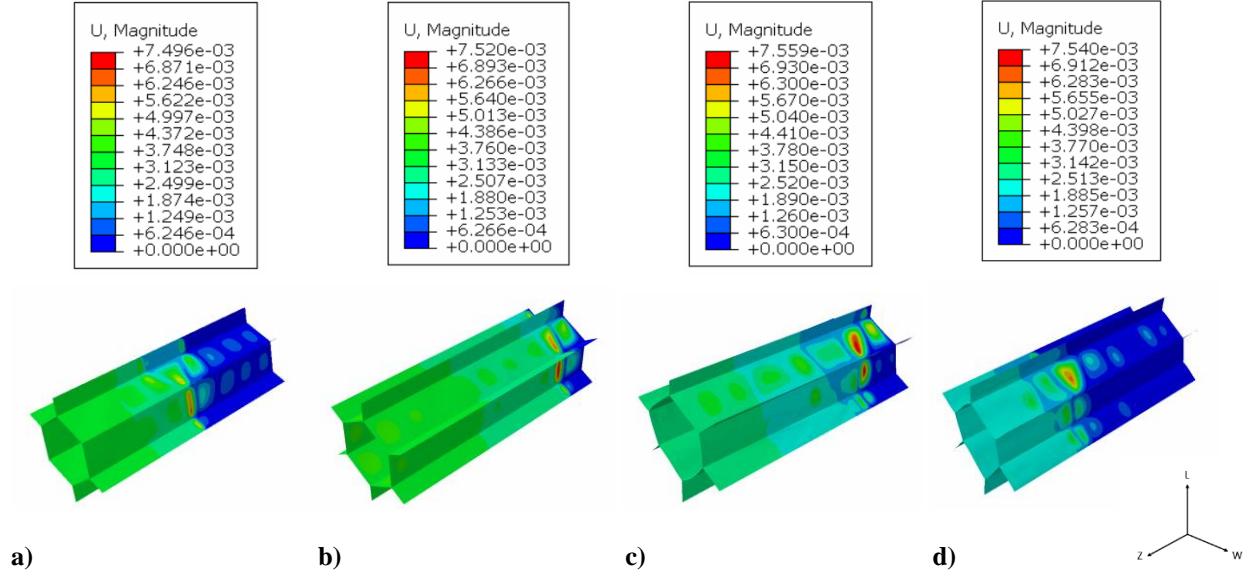
Fig. 16 Contour plots of the magnitude of the displacements prior to the initiation of buckling a) idealized unit cell with average waviness, b) idealized unit cell with peak waviness, c) unit cell from batch B specimens, and d) unit cell from batch R specimens.
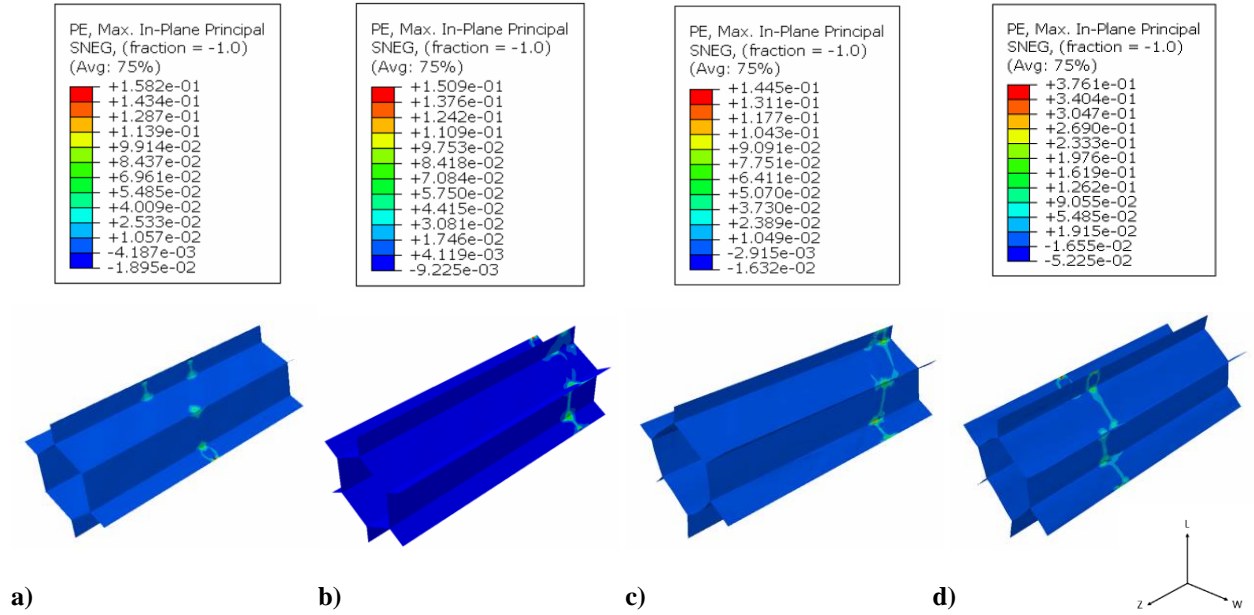

Fig. 17 Contour plots of the plastic strains prior to the initiation of buckling a) idealized unit cell with average waviness, b) idealized unit cell with peak waviness, c) unit cell from batch B specimens, d) unit cell from batch R specimens.

Fig.17 presents contour plots of the plastic strains in the unit cell walls at the load step immediately before the peak load. These results show plastic strains are concentrated in the sharp corner features and propagate across the cell walls at the location of the collapse. In the idealized models, the plastic strains initiate in the double cell walls and propagate across the unit cell. The unit cell model based on the batch B specimen exhibits higher overall plastic strains prior to the collapse of the cell walls explaining the pre-peak hardening behavior observed in Fig 15.
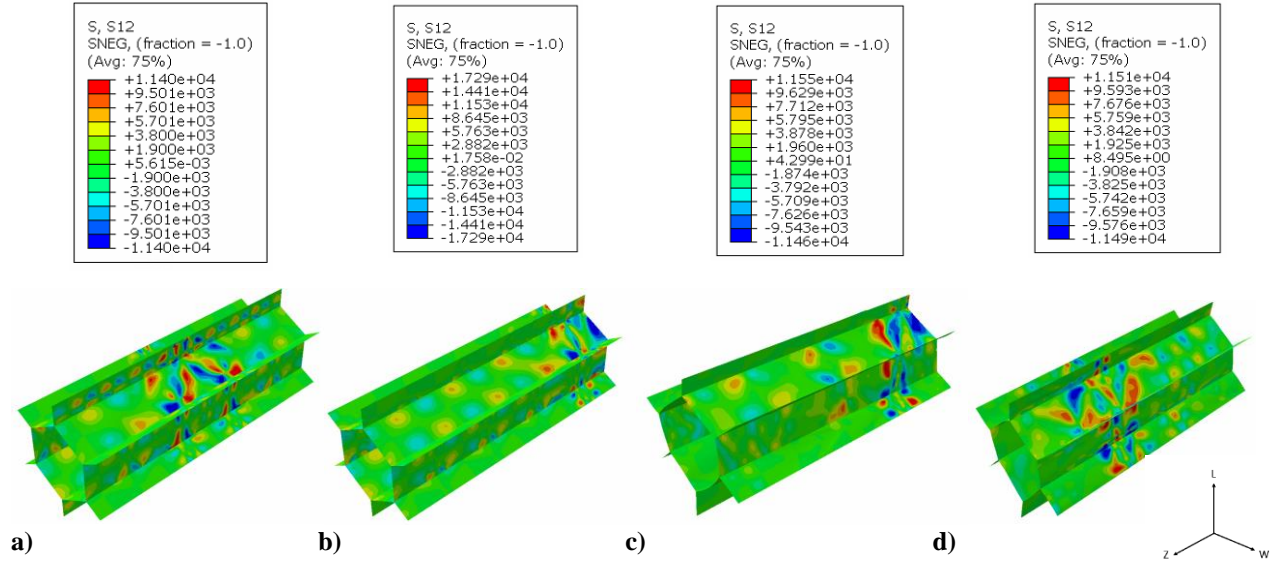
10

Fig. 18 Contour plots of the shear stresses (psi) on the unit cell models prior to the initiation of buckling a) idealized unit cell with average waviness, b) idealized unit cell with peak waviness, c) unit cell from batch B specimens, and d) unit cell from batch R specimens.

Fig. 18 presents the amplitude of the shear stress in the cell walls at load step prior to peak load. These contours exhibit localization of in-plane shear stresses at the regions where the cell wall collapses leading to failure. In the idealized case scaled to the peak waviness and the case from batch B, the shear localization happens closer to the edges indicating presence of edge effects that influences the buckling and the collapse region.

Figs. 19 – 22 plot the amplitude of the deviations of the nodal locations on the cell walls in the direction normal to the surface of the unit cell along a line centered on each cell wall for the batch R and batch B models. The amplitude was arbitrarily set to zero at the mid-height (z=0.4 inch). These plots indicate the cell walls have an inclination with respect to the loading (thickness direction) and a waviness imperfection. Since diametrically opposed cell walls do not have the same inclination it is concluded this is a shape imperfection and not a simply a rotation due to rigid body rotation of the core.

In Fig. 19 the cell collapse location observed in the analysis results coincides with the location of buckling localization, namely in cell wall in 3-4 (Fig. 18c) and corresponds to a local extremum in cell wall waviness. The cell wall inclination was 0.00423 inches over the 0.8 inch model length for the 3-4 single cell wall. Fig. 20 shows that the cell wall inclination is lower in the double cell walls 2-3 and 5-6.

From the nodal position plots in Fig. 21, it is observed that the collapse location for the batch R unit cell coincided with the cell wall in 3-4 location at a local peak in cell wall waviness, consistent the case shown for batch B.

Figs. 23 and 24 plots nodal position normalized by an average mean surface looking specifically at the failing cell wall in each batch (3-4) and the surrounding single cell wall and double cell wall (4-5 and 2-3). The plots show the periodicity in the measured waviness. In batch B the local wavelength at the failure location is 0.050 inches with a max amplitude bounded within ±0.0008 inches. Among the surrounding cell walls the failure location has the shortest wavelength at cell wall 3-4 for batch B between local peaks as well as being out out-of-phase with the surrounding cell walls. Regions with slightly larger amplitudes have both a longer local wavelengths as well as being in-phase with a surrounding cell wall. For the plot of the batch R unit cell the failure locations local wavelength is 0.075 inches with a max amplitude bounded within ±0.0005 inches. Similarly, to batch B the region of failure for the batch R unit cell has the shortest local wavelength at cell wall 3-4 while also being out-of-phase with the surrounding cell walls. Locations in which the cell walls are out-of-phase and have shorter wavelengths will have larger geometric deviations that can explain the localization of the buckling failure.
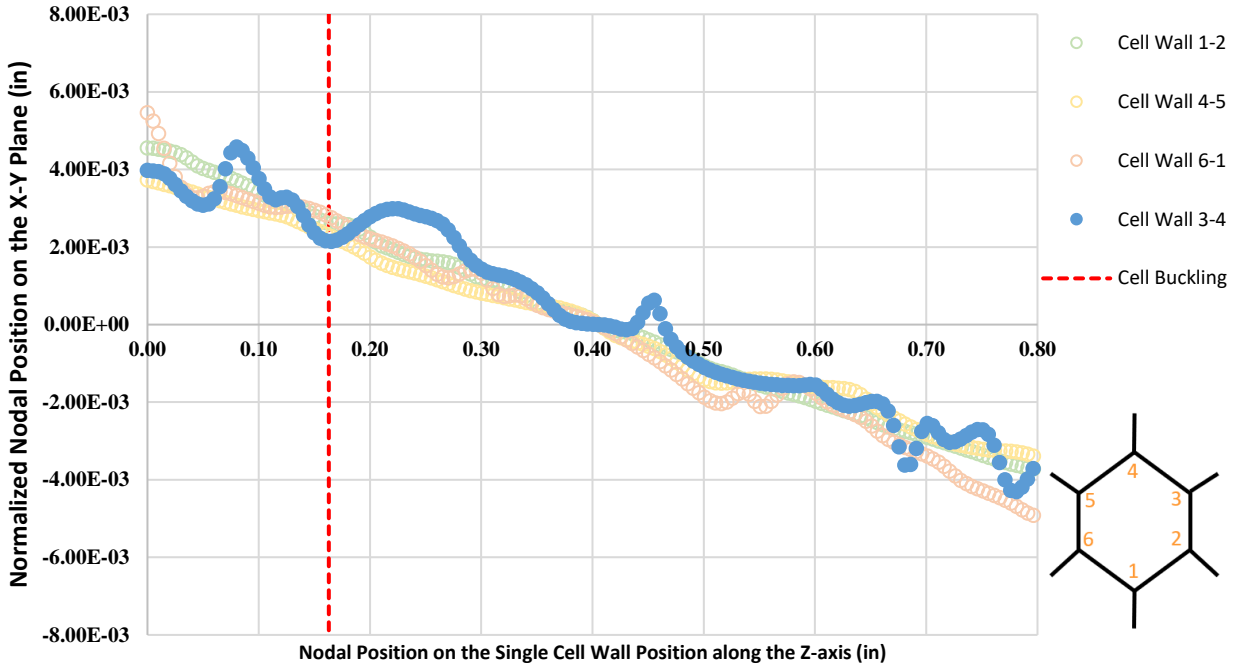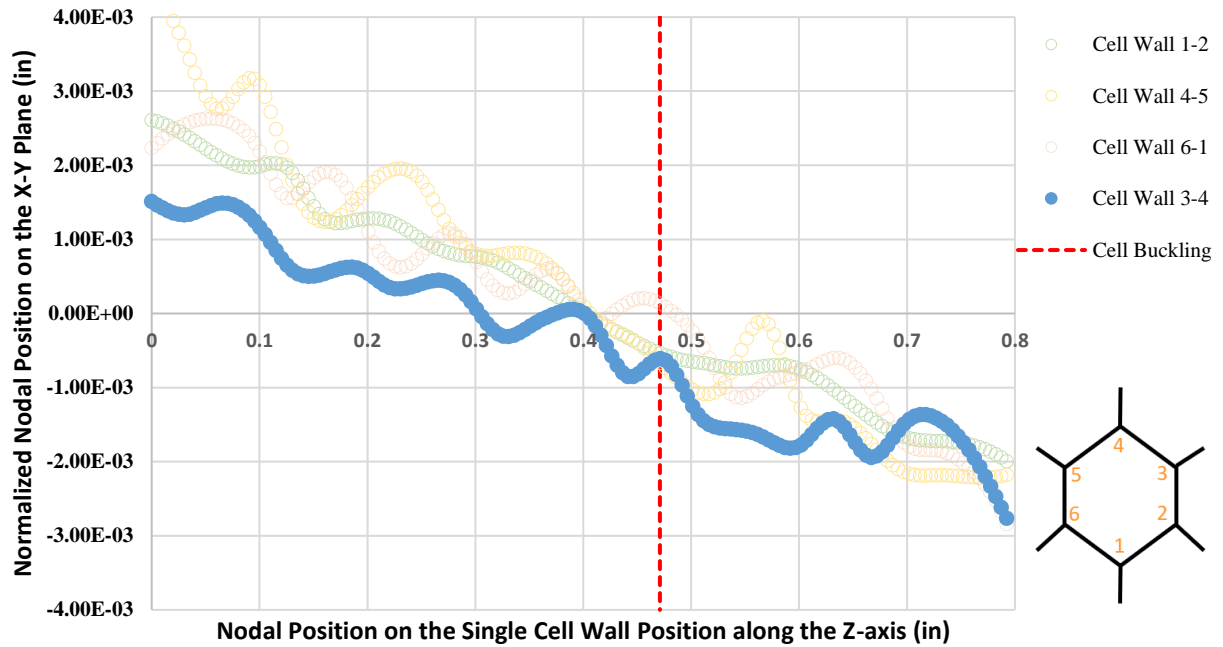
11

Fig. 19 Plot of the nodal position along the center line of the single cell walls for the unit cell model from batch B and the location of cell buckling.

Fig. 20 Plot of the nodal position along the center line of the double cell walls for the unit cell model from batch B.

Fig. 21 Plot of the nodal position along the center line of the single cell walls for the unit cell model from batch R and the location of cell buckling.
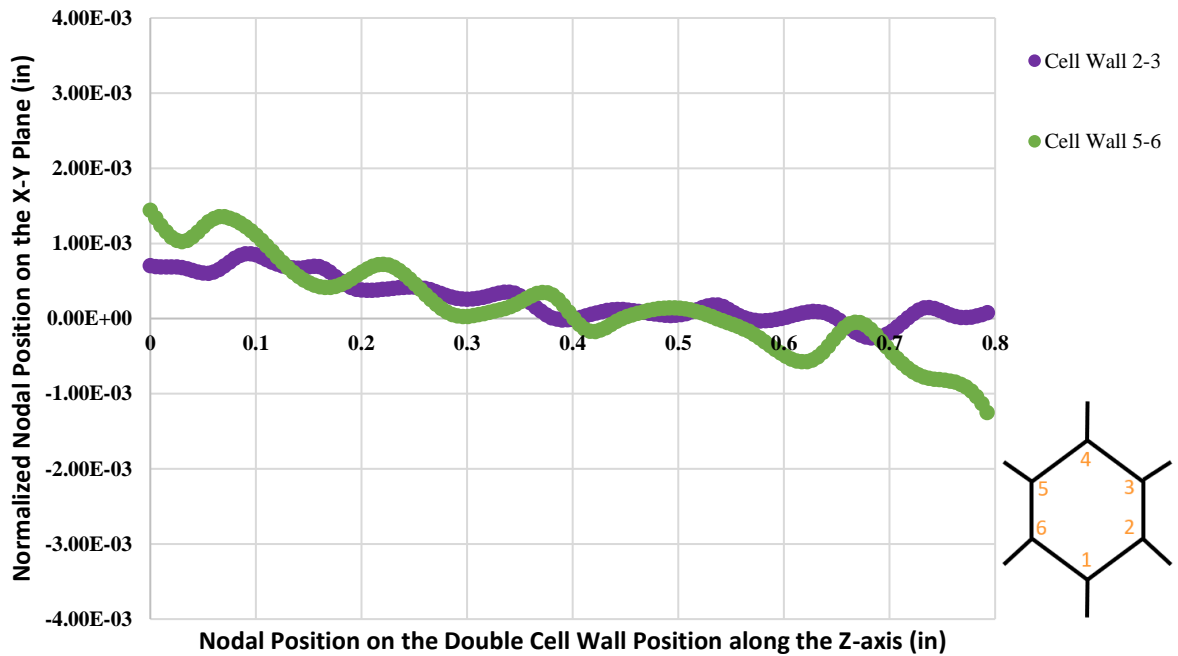

Fig. 22 Plot of the nodal position along the center line of the double cell walls for the unit cell model from batch R.
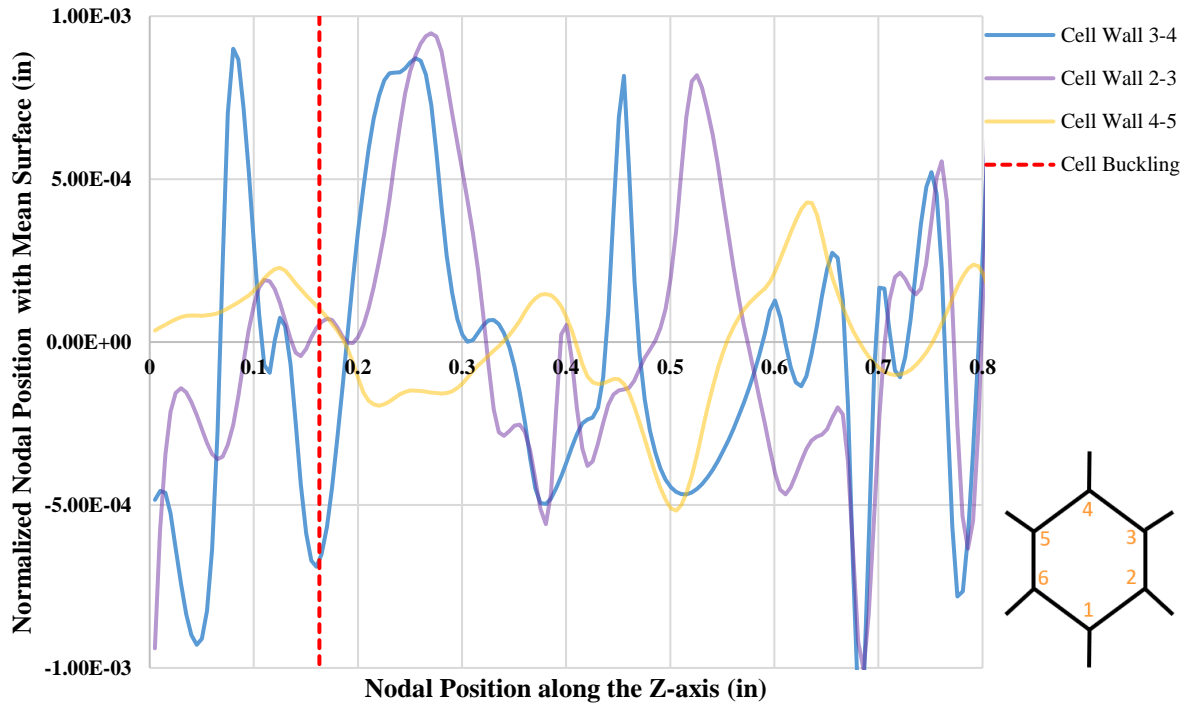
13

Fig. 23 Plot of the nodal position normalized by the mean surface for the unit cell model from batch B.
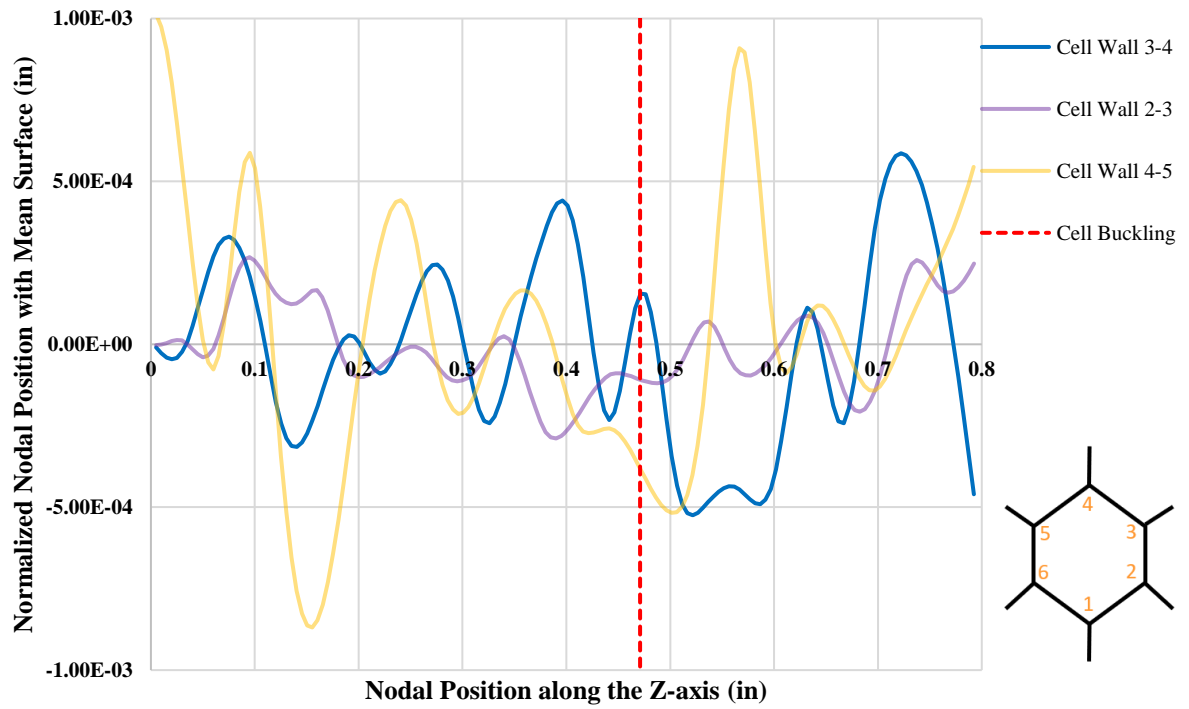

Fig. 24 Plot of the nodal position normalized by the mean surface for the unit cell model from batch R.

VI. Conclusion

This paper establishes methods for geometric reconstruction of CT scan images of aluminum honeycomb cores to quantify the geometric variations and imperfections and for the construction of shell finite element models for analysis. The study compares geometric imperfections of honeycomb cores from two batches of specimens manufactured at different locations with nominally identical materials and overall processing steps (batch B and R). In flatwise compression tests, the two batches showed a significant difference in strength, with batch R having 12.6% higher strength. X-Ray computed tomography (CT) scans of the specimens conducted prior to testing are analyzed and compared to explain the differences in the compression strength. Geometric analysis of the X-Ray CT data shows that there is a quantifiable difference in the cell diameter between batches indicating the honeycomb core were over expanded or under expanded in each batch, respectively. It was also found that the variation in internal angles were similar for the two batches. However, the distributions show batch B has significantly more distorted cells with larger amplitudes (more outliers) than batch R. The out-of-plane cell wall waviness imperfections were larger for the single cell walls compared to the double thickness walls. Finite element models were constructed using the as-manufactured imperfection data and compared to models with idealized imperfections. The models represent a unit-cell with shell elements and were analyzed with a dynamic implicit step to predict the buckling, post-buckling, and crushing response. The unit cell analysis showed that the flatwise compression strength is highly influenced by the peak amplitude and the local wavelength of the imperfection in the cell walls. The location of the collapse of the cell correlates to a local peak amplitude with the smallest local wavelength along the cell wall.

Acknowledgments

References

[1] Liu, Longquan, Hai Wang, and Zhongwei Guan. "Experimental and numerical study on the mechanical response of Nomex honeycomb core under transverse loading." Composite Structures 121 (2015): 304-314.

[2] Petras, Achilles, and M. P. F. Sutcliffe. "Failure mode maps for honeycomb sandwich panels." Composite structures 44.4 (1999): 237-252.

[3] King, William T., et al. "Effects of honeycomb core damage on the performance of composite sandwich structures." Journal of Composite Materials 54.16 (2020): 2159-2171.

[4] Anders, M., et al. "Process diagnostics for co-cure of sandwich structures using in situ visualization." Composites Part A: Applied Science and Manufacturing 116 (2019): 24-35.

[5] Standard, A.S.T.M. "C365-03: Standard test method for Flatwise Compressive Properties of Sandwich cores." Annual Book of ASTM Standards (2003).

[6] Abramian, Anaïs, et al. "Nondestructive Prediction of the Buckling Load of Imperfect Shells." Physical Review Letters 125.22 (2020): 225504.

[7] Chang, S. Grace, Bin Yu, and Martin Vetterli. "Adaptive wavelet thresholding for image denoising and compression." IEEE transactions on image processing 9.9 (2000): 1532-1546.

[8] Grady, Leo. "Random walks for image segmentation." IEEE transactions on pattern analysis and machine intelligence 28.11 (2006): 1768-1783.

[9] Lorensen, W. E. and Cline, H. E., "Marching Cubes: A High Resolution 3D Surface Construction Algorithm," Computer Graphics, vol. 21, no. 3, pp. 163-169, July 1987.

[10] Lerch, Bradley A. "Properties of 5052 Aluminum for Use as Honeycomb Core in Manned Spaceflight." NASA/TM—2018-219753, (2018).

[11] Simulia, Abaqus Analysis User's Guide. Version 2019, 2019.